


RSC-APMN: Random Sea Condition Adaptive Perception Modulating Network for SAR-Derived Marine Aquaculture Segmentation

Jianchao Fan , Member, IEEE, and Qiwen Deng

I. INTRODUCTION

Abstract—The changing marine environment profoundly affects synthetic aperture radar (SAR) imaging quality. And the current deep neural network model cannot consider the variation of environmental factors. As sea conditions intensify, distinct variations in sea surface scattering characteristics emerge, leading to diverse feature distributions in images across different sea conditions, which variability poses constraints on the extraction capabilities of deep learning models. To address the above-mentioned issues, the random sea condition adaptive perception modulation network (RSC-APMN) is proposed to establish a coupled relationship with sea condition levels for adaptive enhancement of SAR imagery and semantic segmentation. Leveraging geographic coordinates and acquisition time of SAR images, RSC-APMN employs the sea condition level assessment method to estimate actual wind speeds and determine sea condition levels. The sea condition adaptive nonlinear decay module adjusts the decay ratio of different regions in SAR images under varying sea conditions based on the grayscale intensity and density characteristics of aquaculture targets, which maximizes the retention of target information while suppressing interference, such as sea clutter. To effectively utilize information from both original and enhanced images and address challenges posed by varying background noise and image blurring due to diffuse or Bragg scattering under different sea conditions, we designed the complex environments omnidirectional perception segmentation module, which ensures robust semantic segmentation in random sea conditions. Experiments demonstrate the effectiveness of the proposed approach based on marine aquaculture under sea conditions levels ranging from 0 to 5, with experimental data composed of GaoFen-3 images from Ningde, Fujian.

Index Terms—Deep learning, marine aquaculture, random sea conditions, synthetic aperture radar (SAR), semantic segmentation.

Manuscript received 18 April 2024; revised 25 June 2024; accepted 15 July 2024. Date of publication 19 July 2024; date of current version 5 August 2024. This work was supported in part by the National Natural Science Foundation of China under Grant 42076184, Grant 41876109, and Grant 41706195, in part by the National Key Research and Development Program of China under Grant 2021YFC2801000, in part by the National High Resolution Special Research under Grant 41-Y30F07-9001-20/22, in part by the Fundamental Research Funds for the Central Universities under Grant DUT23RC(3)050, and in part by the Dalian High Level Talent Innovation Support Plan under Grant 2021RD04. (Corresponding author: Jianchao Fan.)

The authors are with the School of Control Science and Engineering, Dalian University of Technology, Dalian 116023, China (e-mail: fjchao@dlut.edu.cn; qiwendeng@mail.dlut.edu.cn).

The code of this work will be available at <https://github.com/fjc1575/Marine-Aquaculture/RSC-APMN> for the sake of reproducibility.

Digital Object Identifier 10.1109/JSTARS.2024.3430939

WITH the ongoing growth of the world's population, the manner in which marine aquaculture interacts with ecosystems will become increasingly crucial in ensuring the long-term stability of food sources and social well-being [1]. By 2020, the total area of marine aquaculture nationwide had reached 1, 173, 249.22 hectares, showing a spatial distribution characteristic of Denser North and Sparser South [2]. However, with the development of aquaculture, improper planning and regulation may damage offshore ecosystems and adversely affect their ability to provide the ecological services needed for the sustainable development of marine aquaculture [3], such as inorganic nitrogen imbalanced and nutrient composition of seawater imbalanced [4], and biodiversity degradation [5]. To achieve a balance between economic development and ecological conservation, there is an urgent need for effective monitoring of the marine aquaculture industry to achieve sustainable development [6]. In recent years, China's marine microwave remote sensing satellite technology has made a major breakthrough in the identification of marine environmental elements and targets [7], and has the advantages of large coverage and strong timeliness, which is of great significance to the scientific management of aquaculture and the protection of marine ecological environment [8], [9]. Compared to optical satellites, synthetic aperture radar (SAR) satellites are characterized by their independence from lighting conditions, high resolution, and superior penetration capabilities [10], [11].

Marine aquaculture mainly includes two types: raft and cage aquaculture. Raft aquaculture is composed of multiple buoys, boards, and mooring systems [12]. Today, most marine aquaculture uses gravity-based cage systems, which use heavy objects to maintain the shape of the net and are connected to floating structures on the water's surface [13]. Therefore, these two methods exhibit distinct characteristics in remote sensing images. With advancements in artificial intelligence technology, there have been notable strides in extracting information related to marine aquaculture using deep learning methods. Liu et al. [14] proposed an SRUnet model based on a Swin transformer, utilizing medium-resolution remote sensing images to extract nearshore raft aquaculture areas. Cui et al. [15] employed an end-to-end FCN-based model for extracting raft aquaculture areas, successfully addressing the adhesion phenomenon. Combining segmentation networks and nonsubsampling contourlet transform,

Zhang et al. [16] extracted marine raft aquaculture areas using Sentinel-1 images. To tackle issues arising from turbid water environments and varying buoy scales in aquaculture regions, Su et al. [17] modified the U-Net network using dual-channel and residual hybrid dilated convolution blocks, constructing RaftNet to enhance the accuracy of target extraction. Moreover, Zhou et al. [18] proposed an invariant information differentiable feature clustering network for extracting information from marine aquaculture, aiming to enhance spatial continuity and reduce the impact of speckle noise. To address the issues of interclass confusion and intraclass disconnection that may arise in self-supervised learning with large datasets, Fan et al. [19] proposed a self-supervised feature fusion-based semantic segmentation method for monitoring marine aquaculture in SAR images. To fully utilize the phase information in PolSAR data, Fan et al. [20] constructed a complex-valued convolutional neural network for the recognition of marine aquaculture to improve detection accuracy. With the development of intelligent extraction in marine aquaculture, to overcome the dependence of deep learning on labels, Wang et al. [21] and Zhou et al. [22], respectively, proposed an incremental double unsupervised deep learning approach and an unsupervised mutual-information-differentiable feature clustering model for extracting information from marine aquaculture without requiring any labels.

However, current intelligent extraction methods often overlook the potential impact of dynamic environmental changes, such as sea conditions and wind speed on the performance of deep learning networks, resulting in insufficient environmental adaptability of the models, leading to a decrease in extraction accuracy or even invalid. Jiang et al. [23] pointed out that improving the accuracy of remote sensing of oceanographic information under severe sea conditions is one of the current main research directions. In SAR measurements, sea surface backscatter consists of resonant Bragg-wave backscattering and non-Bragg scattering induced by breaking waves, which is directly affected by sea surface roughness and wind field [24]. While, backscatter is also subject to the influence of various environmental factors, including swell, and sea temperature, among which wind speed stands out as the primary influencing parameter [25]. According to scattering theory, short-period waves on the sea surface are modulated by the wind, resulting in periodic streaks of light and dark on the image [26]. Coastal zones used for marine aquaculture are mostly characterized by complex terrain, where wave refraction and diffraction frequently occur, and the sea surface wind field undergoes drastic changes in this region. As the sea conditions rise, the sea surface scattering effect intensifies, making the target signal easily submerged in strong sea clutter signals [27], [28]. Moreover, due to the long satellite re-entry cycle [29], the randomness of the marine environment, and the time limit of monitoring tasks, it is of great significance to carry out marine aquaculture information extraction under random sea conditions.

When the sea condition level is close to B_0 , as shown in Fig. 1(a), with no or low wind speed, the sea surface can be regarded as a quasimirror. In this case, the electromagnetic waves emitted by the side-looking radar are reflected off the sea surface, resulting in a very weak echo signal. At the same

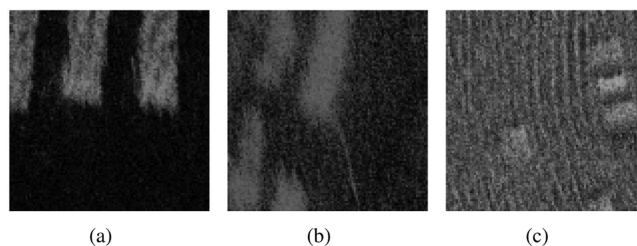


Fig. 1. Marine aquaculture under random sea conditions. (a) B_0 -level marine aquaculture SAR image. (b) B_3 -level marine aquaculture SAR image. (c) B_5 -level marine aquaculture SAR image.

time, the echo signal of the floating raft as an artificial target is stronger than the sea surface. Therefore, the remote sensing images have a higher signal-to-noise ratio, which makes the target area better identifiable and presents a regular shape. As the sea condition level gradually increases to around B_3 , as shown in Fig. 1(b), the sea surface waves are generated under the action of wind, and the sea surface roughness changes, thus changing the radar sea surface backscattering intensity. At the same time, when a large number of scattering elements are within the same resolution cell, the scattering intensity will have a weighted impact on each scattering point, resulting in image blurring. When the sea condition level continues to rise to about B_5 , as shown in Fig. 1(c), the backscatter may form alternating bright and dark gray stripes in SAR images due to modulation by the sea waves. Meanwhile, the increasing sea conditions may bring disturbances, such as sea foam, breaking waves, and airborne mist, making the identification of marine aquaculture extremely challenging. It is important to note that the gray stripes are primarily influenced by the sea wind, but not all SAR remote sensing images will display consistent gray stripe features corresponding to the wind. These features are more pronounced under unstable atmospheric conditions and may sometimes be completely absent under stable conditions. Furthermore, atmospheric gravity waves or internal ocean waves may also produce features similar to wind stripes, affecting the extraction of sea surface targets.

To address the SAR target detection problem in random sea conditions, numerous scholars analyze the statistical characteristics of background noise to distinguish clutter and target information. Constant false alarm rate (CFAR) is a mainstream technique used for target detection and clutter suppression, which relies on probability distribution functions to establish the optimal segmentation threshold between targets and background, enabling target detection in strong clutter backgrounds [30], [31]. Gao et al. [32] utilized the reciprocal of the gamma distribution to describe the texture components of sea clutter in nonuniform backgrounds, and derived a statistical model to achieve the CFAR. Yang et al. [33] proposed a new orthogonal projection-based CFAR detector, which effectively suppressed sea clutter by constructing a clustering subspace using data vectors of adjacent distance units and projecting signals from the region to be detected into the subspace. In order to improve the detection performance of sea clutter samples in the multitarget

environment, Ai et al. [34] proposed a robust CFAR detection method for Gaussian clutter anomalies in SAR images based on truncated maximum likelihood estimation. Aiming at the problem that wave shadows and sea peaks make small target detection difficult under low sweep angles and high sea conditions, Xie et al. [35] proposed a controllable CFAR detector based on three radar echo phase characteristics. Fan et al. [36] proposed a parameter estimation method based on variable interval to deal with the influence of anomalous scattering unit echo with the increase of sea wave height, which is suitable for the problem of target detection performance when using Pareto distribution to describe the statistical characteristics of sea clutter amplitude. Xie et al. [37] proposed a target detection algorithm based on the maximum eigenvalue of the sample covariance matrix to address the limited performance of model-driven CFAR detectors in complex and dynamic marine environments. However, the method of adapting the background noise distribution in simulated images through statistical analysis to suit dynamic environments as described previously requires complex manual parameter design and has certain limitations when dealing with complex scenes. Deep learning demonstrates promising potential in capturing nonlinear relationships [38], [39], [40] under random sea conditions, owing to its robust capability in nonlinear mapping and approximation. However, current research in extracting aquaculture information under random sea conditions remains in its early stages. In this field, the adverse effects of random sea conditions on image formation have not been adequately addressed. There is a lack of effective methods to mitigate the impact of varying sea conditions on the changes in complex scattering characteristics and their influence on image feature distributions. This deficiency significantly contributes to the decline in extraction accuracy. Therefore, we are conducting research using deep learning methods to enhance and extract aquaculture information in SAR image under random sea conditions.

Based on the above-mentioned research, this article proposes a random sea condition adaptive perception modulation network (RSC-APMN). The net is designed to establish a monitoring system for marine aquaculture targets under random sea conditions, and its feasibility has been verified by experiments under real sea conditions of 0–5. It solves the problems of sea conditions grading based on time and space information of SAR images, adaptive improvement of signal-to-noise ratio, and background noise of SAR images under random sea conditions, and significant degradation of performance of traditional semantic segmentation model under random sea conditions. The entire net consists of three parts, including the sea condition level assessment (SCLA) module, the sea condition adaptive nonlinear decay (SCAND) module, and the complex environments omnidirectional perception segmentation (CEOPS) module. First, the SCLA module utilizes the acquisition time and geographical location information of SAR images to retrieve the actual sea condition levels of the marine environment. Second, the SCAND module can preliminarily eliminate ocean background noise and enhance the image signal-to-noise ratio by establishing the relationship between gray value and distribution density of marine aquaculture targets and sea condition levels.

Furthermore, considering the characteristics of the global distribution of background noise and mutual interference with the target under random sea conditions, a CEOPS module is designed for extracting marine aquaculture under random sea conditions, which enhances the model's focus on the effective regions retained in the modulation results within the original image, maintains a large receptive field of the model, and promotes omnidirectional communication and weighted fusion of multidimensional features. Effectively improve the filtering of background noise in complex scenarios and the fusion processing ability of target semantic information and spatial information. This article makes the following contributions.

- 1) A random sea condition adaptive perception modulating network is proposed for marine aquaculture under random sea conditions, with levels ranging from 0 to 5. Comprising SCLA, SCAND, and CEOPS modules, the network utilizes the spatiotemporal information of SAR images to determine sea condition levels, adaptively enhances image quality, integrates original data with modulation results, and facilitates multidimensional information omnidirectional transfer and fusion for robust extraction in dynamic marine environments, thus advancing aquaculture monitoring.
- 2) Based on the analysis of the variation of the gray scale and density of the marine background and targets with the sea conditions, a SCAND module is proposed to enhance the image quality. It processes information decay rates differently in different image regions based on sea condition levels, effectively suppressing background noise, such as sea clutter while preserving target information for subsequent target extraction. In addition, an image comprehensive modulation quality (ICMQ) metric is designed for evaluation.
- 3) The CEOPS module is tailored to extract information in random sea condition environments, which merges original data and modulation results to offer comprehensive features. In view of the global distribution of ocean noise, it maintains a large receptive field to capture long-range information and employs a pyramid structure with multi-scale information fusion and feature-weighted fusion to learn the importance and effectiveness of different sea conditions features, which prevents the decline in performance of semantic segmentation models under random sea conditions.

The rest of this article is organized as follows. Section II proposes the related work related to the research direction of this article and provides prior knowledge. Section III proposes the proposed RSC-APMN model in detail for SAR image marine aquaculture under random sea conditions. Section IV shows the experimental results of the work. Finally, Section V concludes this article.

II. PRELIMINARY WORK

A. BiFP Network

In random sea conditions, traditional deep semantic segmentation networks with small receptive fields and weak integration

of contextual information may be affected by phenomena, such as sea clutter background noise, and image blurring caused by changes in sea conditions and surface roughness. Tan et al. [41] proposed a simple yet effective weighted bidirectional feature pyramid (BiFP), as shown in Fig. 2, which combines top-down and bottom-up feature propagation with multiscale weighted fusion to enhance the model's understanding and expression of input data.

Due to the distinct resolutions of different input features, they typically make unequal contributions to the output features. Based on this concept, BiFP proposed a weighted fusion method

$$O = \sum_i \frac{\omega_i \cdot I_i}{\epsilon + \sum_i \omega_i} \quad (1)$$

where O represents the output features, I_i denotes the input features, ω_i represents a learnable weight, which can be scalars, vectors, or multidimensional tensors, and $\epsilon = 0.0001$ is a small value used to mitigate numerical instability.

B. Kernel Density Estimation

General probability density estimation methods can be broadly categorized into two types: parametric estimation and nonparametric estimation. Among them, nonparametric estimation involves estimating the entire probability density function based on the properties of a large sample when the distribution form of the sample data is unknown and difficult to describe using simple functions. Gaussian kernel density estimation $f_h(\cdot)$ is a nonparametric method used to estimate the probability density function of a random variable

$$f_h(x) = \frac{1}{n} \times \sum_{i=1}^n K_h(x - x_i) = \frac{1}{nh} \times \sum_{i=1}^n K\left(\frac{x - x_i}{h}\right)$$

$$K(u) = \frac{1}{\sqrt{2\pi}} e^{-\frac{u^2}{2}} \quad (2)$$

where n is the number of sample data points, h is the bandwidth, which is a parameter controlling the smoothness of the estimation, x_i represents the sample data points, and $K(\cdot)$ is the kernel function, with the gaussian kernel function being selected in this context.

III. PROPOSED METHOD

To construct an adaptive extraction model for aquaculture information under random sea conditions, actual sea condition levels are obtained using latitude, longitude, and time. The images are then adaptively enhanced, and a semantic segmentation module handles global background noise to extract target information. This method can be summarized into three parts, as depicted in Fig. 3. The first part, as shown in Fig. 3(a), involves obtaining measured wind speeds and generating sea condition levels based on latitude and longitude information and acquisition time of SAR images. The second part, as shown in Fig. 3(b), establishes a coupling relationship between sea condition levels and SCAND module to adaptively mitigate background noise produced in SAR images under different sea conditions. As

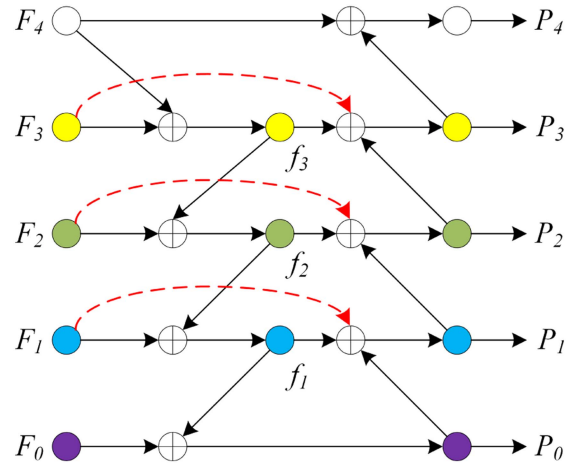


Fig. 2. Structure of BiFP, which includes: Bidirectional information flow allows for the transmission of information in both upward and downward directions. The weighted fusion mechanism enhances the capability of feature representation.

Algorithm 1: RSC-APMN Model.

Require : $u_i, P_i, \kappa, \epsilon$
 $B_i \leftarrow SCLA(\{P_i\})$
 $u'_i \leftarrow GrayscaleEstimation(\{u_i, B_i\})$
 $u''_i \leftarrow DensityEstimation(\{u'_i\})$
for True **do**
 Initialize : θ_g
 for $t = 0$ **to** κ **do**
 Output $\leftarrow CEOPS(\{g(u_i; u'_i; u''_i; \theta_g)\})$
 $L \leftarrow L_{BCE}(\{Output\})$
 end for
 Out Output
 if $\delta < \epsilon$ **do**
 break
end for

shown in Fig. 3(c) and 3(d), the third part involves designing a CEOPS module tailored for aquaculture under random sea conditions to obtain the extraction results of aquaculture.

A. RSC-APMN Model

The specific issues addressed by this network are as follows. Assuming $Input_0 = \{u_1, u_2, \dots, u_n\}$, $u_i \in R^{H \times W \times 1}$ is a dataset composed of n high sea condition images. First, wind speed information is obtained from the European centre for medium-range weather forecasts (ECMWF) based on shooting time $t_i, i \in \{1, \dots, n\}$, longitude and latitude $P_i, i \in \{1, \dots, n\}$ of the high sea condition SAR images, and the corresponding sea condition level $B = \{B_1, B_2, \dots, B_n\}$ is obtained from the Beaufort scale. Considering the accuracy of ECMWF climate data, in order to avoid missing climate information in some images, an SCLA module has been designed. Please refer to section B for details.

In addition, in order to highlight marine aquaculture targets and suppress background noise to its minimum darkness, the

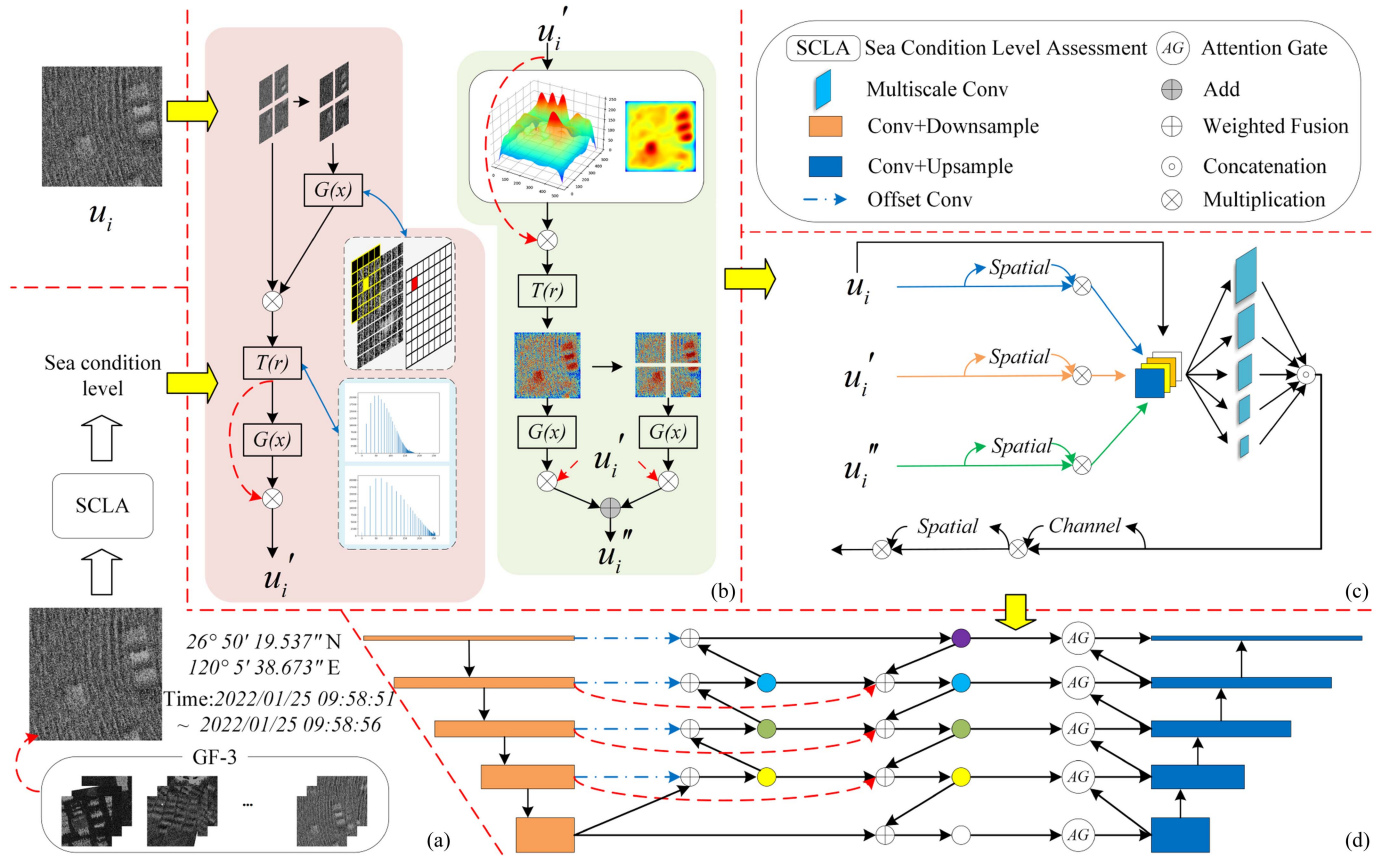


Fig. 3. Structure of RSC-APMN model starts from: (a) SCLA module, which estimates the actual sea condition levels by combining geographic coordinates and time data, (b) SCAND module, which includes two parts: grayscale intensity estimation and density estimation, and (c) ~ (d) CEOPS module.

SCAND module is designed based on the characteristics of SAR images under different sea condition levels. Because of the influence of abnormal pixels, the module uses a sliding window of different sizes to perform grayscale intensity statistics to calculate the decay ratio on each image, enhancing regions with higher grayscale values in the enhanced image. Due to the use of ratio calculation for stretching, each part of the image information is subjected to varying degrees of attenuation. To enhance the contrast between the target area and the ocean background, a histogram equalization method is used to further highlight the target information. At this stage, while the target regions exhibit improved contrast against the marine background compared to the original image, minor background noise in certain random marine scenarios has also been enhanced. For instance, in $B5$ conditions, there are bright stripe noise caused by Bragg scattering, which has not been fully suppressed. To further enhance image separability, grayscale intensity estimation is recalibrated based on sea condition levels, and decay ratio indices are adjusted accordingly to accommodate the complexities of each marine environment. Conducting grayscale intensity statistics on the histogram-equalized images and adjust the decay ratio to obtain $r_1, r_1 \in R^{H \times W \times 1}$ based on the sea condition level $B_i, i \in \{1, \dots, n\}$. After that, multiply the ratio r_1 with the histogram equalized image to obtain the first set of modulation result images $\text{Input}_1 = \{u_1', u_2', \dots, u_i'\}$.

To address the striped noise with higher grayscale values caused by sea clutter and background noise that cannot be completely eliminated in Input1, SCAND employed the Gaussian kernel density estimation method to estimate the density of Input1, resulting in a probability density map $\mathcal{D} = \{d_1, d_2, \dots, d_n\}$. Due to the smoothing nature of the Gaussian kernel function, when grayscale values exhibit significant variations in the image, the changes in density estimation are not very pronounced and the presence of low grayscale value pixels can propose errors, as it is commonly assumed that these low grayscale value pixels do not belong to the target region. So, SCAND module multiply u_i' by the probability density map d_i to create a new probability density image, which will be used for subsequent distribution statistics and decay ratio $r_2, r_2 \in R^{H \times W \times 1}$ calculations. The decay ratio calculation method remains consistent with the previous approach. It is worth noting that, in this context, to mitigate mutual interference between the density distributions of target regions, SCAND module employ two ratio calculation modes: one is a global mode, and the other is divided into four parts. Ultimately, using a weighted averaging approach to combine the results of these two modes to obtain $\text{Input}_2 = \{u_1'', u_2'', \dots, u_i''\}$.

In order to achieve semantic segmentation in random sea conditions and effectively utilize valuable feature information from the outputs of the SCAND module, this article

proposes CEOPS module. Tailored for the specific task of random sea condition images, this network incorporates a three-input attentional multiscale convolution mechanism based on convolutional block attention module [42] at the input, focusing on valuable spatial areas within u'_i and u''_i , and extracting multiscale target information from the images. During the feature extraction stage, expanding the receptive field through dilated convolutions helps the network better understand the global feature information of the image and effectively suppresses the background noise distributed globally. In addition, to improve the model's precise localization of target features and the filtering effect of background features, offset convolutions are used to select the feature extraction results at each layer. Simultaneously, the introduction of a BiFP structure facilitates the transmission and weighted fusion of multidimensional feature information within the model, thereby improving the model's understanding of object structures and semantics, and effectively avoiding information loss during transmission. In each layer of the decoding part, the attention gate mechanism is introduced to fuse the multidimensional results generated by the BiFP, enhancing the model's target recognition capability under random sea conditions.

B. SCLA Module

In this article, actual wind speeds are retrieved based on the geographic coordinates and acquisition time of the image, using ERA5 data from ECMWF, which comprises global atmospheric reanalysis data spanning hourly increments from 1959 to the present, covering atmospheric, land, and ocean climate variables on a global scale with a 30 km grid resolution (0.25°). It can be obtained online.¹ However, to address the absence of environmental data, the SCLA module is designed to estimate missing environmental information. In addition, sea conditions typically refer to the surface wave dynamics influenced by the strength of the wind. The Beaufort scale is widely recognized in maritime circles as a standardized measure for assessing wind speeds on land and at sea [43]. Furthermore, it has been expanded to include evaluations of wave height and overall sea conditions, and has been endorsed by multiple maritime authorities.

This module employs the Delaunay triangulation algorithm to process a discrete set of data points, ensuring that the closest three points form triangles where no segments intersect. Furthermore, the triangulation ensures that within the circumscribed circle of any triangle, no additional data points exist, and among all possible triangulations, it selects those triangles with the largest minimum angle. During interpolation calculations, this module selects the triangle with the smallest area that contains the interpolation point as the computation domain, and utilizes the barycentric coordinates of the triangle's vertices for interpolation within the triangle

$$v = \lambda_1 A + \lambda_2 B + \lambda_3 C \quad (3)$$

where, v represents the estimated wind speed, A , B , and C represent the values at the three vertices of the triangle, λ_1 , λ_2 ,

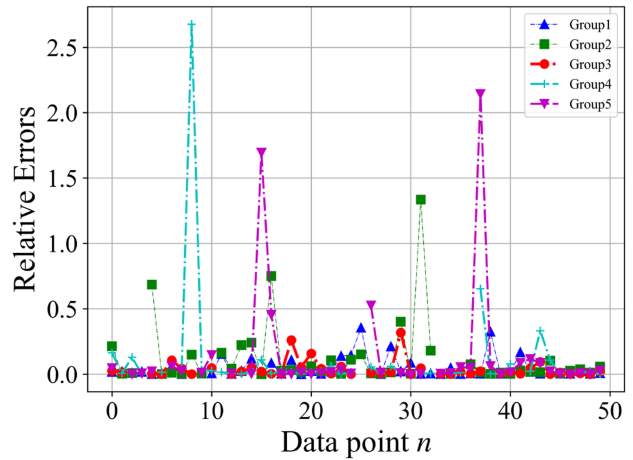


Fig. 4. Relative error between the interpolated results and the ground truth. Five sets of data, each containing 50 samples, were selected to compute the relative errors between interpolated values and ground truth. It is evident that the vast majority of data points exhibit relative errors close to zero, remaining within the range of 0–0.1. Only a small minority of samples show relative errors exceeding 0.2, typically falling between 0.2 and 0.5.

and λ_3 , respectively, denote the ratios of the Euclidean distances from the interpolation point to each vertex relative to the total distance, satisfying $\lambda_1 + \lambda_2 + \lambda_3 = 1$.

To validate the effectiveness of the method, interpolation computations were conducted on randomly selected sets of wind field data. Each set consisted of 50 samples, and relative errors between each sample and the ground truth were computed. As shown in Fig. 4, it is evident that only a small minority of relative errors exceed 0.2. The majority of interpolated results maintain relative errors below 0.1, overall demonstrating the effectiveness of this interpolation estimation method. Finally, compare the obtained wind speed v (m/s) with the Beaufort wind levels table to determine the sea condition level Bn .

C. SCAND Module

Given the dynamic changes in the marine background of SAR images under different sea conditions, this study proposes the SCAND module by analyzing two key aspects: the grayscale intensity and distribution density of targets and backgrounds under different sea conditions. This module can adaptively attenuate the information in different regions of SAR images according to the sea condition levels, effectively enhancing the contrast between aquaculture targets and the marine background, and significantly improving the image's segmentation capability. The SCAND module mainly consists of two main parts: grayscale intensity estimation and density estimation

$$\begin{aligned} u'_i &= F_1(\hat{u}_i) \odot u_i \\ u''_i &= F_2(u'_i) \odot u'_i \end{aligned} \quad (4)$$

where F_1 and F_2 represent grayscale intensity estimation and density estimation, respectively, u_i represents the input random sea condition SAR image, u'_i and u''_i represent the output result of grayscale intensity estimation and density estimation, respectively. \hat{u}_i represents the effective information retained

¹[Online]. Available: <https://cds.climate.copernicus.eu/#/home>

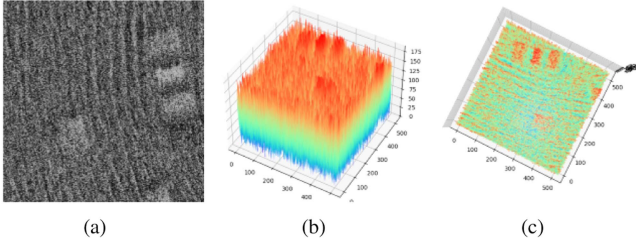


Fig. 5. 3-D visualization of high sea condition SAR images. (a) Source SAR image. (b) and (c) are 3-D visualization images.

after normalizing the input image u_i , which is greater than 0.5. It stems from extensive experiments indicating that in random sea conditions, target regions typically exceed the normalized mean. Such preservation not only reduces computational complexity but also enhances the significant variation in decay rates across different regions.

1) *Grayscale Intensity Estimation*: As the sea condition level increases, as shown in Fig. 5, it is influenced by local sea surface winds, resulting in changes in the distribution of microscale waves on the sea surface and changes in sea surface roughness, thereby affecting the intensity of radar backscattering. At the same time, sea winds will generate wind-induced surface waves, causing the sea surface microwave scattering to transition to Bragg scattering. This change can affect or even obscure the echo information of aquaculture targets, which is recorded in the form of grayscale values on SAR images, resulting in reduced contrast between targets and backgrounds, thereby affecting the visibility and separability of the images.

It is observed that the grayscale values within the target area remain higher than the background. Furthermore, in comparison to sea clutter noise, certain portions of the sea clutter exhibit grayscale values that are close to, equal to, or even higher than those of the target area. However, upon closer examination of their distribution characteristics, it can be noted that the high grayscale information within the sea clutter presents in elongated streak-like patterns, far less dense than the grayscale information within the target area. So, in order to reduce the mutual interference of different scattering targets within the image u_i , partition the input image into four parts: upper-left, upper-right, lower-left, and lower-right.

However, under random sea conditions, while the contrast of SAR images and the structure of aquaculture targets may be affected by the sea conditions, the grayscale values of most targets consistently remain higher than the background. In addition, certain parts of the bright-dark striped patterns generated by wind-induced surface waves may approach, equal, or even exceed the grayscale values of target areas, but their slender image distribution characteristics are far less dense in high grayscale information compared to aquaculture targets. Based on the above-mentioned characteristics, a grayscale-based variable sliding window decay ratio calculation method $G(\cdot)$ has

been designed

$$G(x) = \begin{pmatrix} G^{11} & G^{12} & \dots & G^{1j} \\ G^{21} & G^{22} & \dots & G^{2j} \\ \vdots & \vdots & \ddots & \vdots \\ G^{i1} & G^{i2} & \dots & G^{ij} \end{pmatrix}. \quad (5)$$

The G^{ij} is given as follows:

$$G^{ij} = \frac{\frac{1}{k \times k} \sum x[p, q] - M_{\min}}{M_{\max} - M_{\min}}$$

$$p \in \left[i - \frac{k-1}{2}, i + \frac{k-1}{2} \right]$$

$$q \in \left[j - \frac{k-1}{2}, j + \frac{k-1}{2} \right] \quad (6)$$

where x represents the input of grayscale intensity estimation, G^{ij} represents the pixel decay ratio at the i th row and j th column of the input x , k represents the size of the sliding window, set to 5, 11, 21, and 31 in this study, and then the four results are weighted fused. $x[p, q]$ represents the pixel value at p th row and q th column of x . M_{\min} and M_{\max} are, respectively, the minimum and maximum values of $\frac{1}{k \times k} \sum x[p, q]$.

After undergoing information attenuation by the ratio $G(\cdot)$, SCAND module employ histogram equalization $T(\cdot)$ to enhance the contrast of the processed image

$$s = T(r) \quad (7)$$

where r represents the initial pixel value, and s represents the pixel value after histogram equalization. The calculation method for $T(\cdot)$ is as follows. Assuming the distribution function of the random variable s is represented by F_s

$$F_s = \int_0^s p_s(s) ds = \int_0^r p_r(r) dr \quad (8)$$

$$p_s(s) = \frac{F_s(s)}{ds} = \frac{d \left[\int_0^r p_r(r) dr \right]}{ds} = p_r(r) \frac{dr}{ds} = p_r(r) \frac{dr}{dT} \quad (9)$$

$$s = T(r) = \int_0^r \frac{p_r(r)}{p_s(s)} dr = 255 \int_0^r p_r(r) dr \quad (10)$$

where $p_r(\cdot)$ is the probability density function of the normalized input image, and $p_s(\cdot)$ is the probability density function of a uniform distribution from 0 to 255. Based on the above-mentioned method, the grayscale intensity estimation formula $F_1(\cdot)$ is defined

$$\begin{aligned} u'_i &= r_1 \odot u_i \\ &= F_1(\hat{u}_i) \odot u_i \\ &= G \left(\begin{pmatrix} T(G(\hat{u}_i^{11}) \odot u_i^{11}) & T(G(\hat{u}_i^{12}) \odot u_i^{12}) \\ T(G(\hat{u}_i^{21}) \odot u_i^{21}) & T(G(\hat{u}_i^{22}) \odot u_i^{22}) \end{pmatrix} \right)^n \odot u_i \end{aligned} \quad (11)$$

where u'_i represents the original image u_i enhanced through grayscale intensity estimation, r_1 represents the decay rate calculated after grayscale intensity estimation, \hat{u}_i^{11} , \hat{u}_i^{12} , \hat{u}_i^{21} , and

\hat{u}_i^{22} , respectively, represent the four equal parts of upper left, upper right, lower left, and lower right of \hat{u}_i , which aims to reduce mutual interference among multiple targets within the image. To effectively suppress background noise and preserve target regions under different sea conditions, experiments were conducted to determine the optimal hyperparameters n . Results indicated that when the sea condition level is below $B3$, $n = 0.6$. When the sea condition level is equal to 4, $n = 2.8$. And when the level is equal to 5, $n = 1.8$.

2) *Density Estimation*: When performing kernel density estimation on images, the bandwidth h of the density function $f_h(\cdot)$ controls the window width, affecting the accuracy and sensitivity of the estimate. An excessively large bandwidth leads to over smoothing of the estimate, resulting in a density plot with insignificant variations. Conversely, an excessively small bandwidth results in estimates that are overly sharp and sensitive to noise, making them prone to disturbance by outliers and yielding inaccurate results. By considering the influence of all data points on the bandwidth, kernel function $K(\cdot)$ can mitigate the disturbance caused by outliers. Moreover, as the sample size tends toward infinity, the estimate approaches the true probability density function without bias. Therefore, the mean integrated squared error (MISE) method can be used to select an appropriate bandwidth h .

$$\text{MISE}(h) = E \left[\int (\hat{f}(x) - f(x))^2 dx \right] \quad (12)$$

where $\hat{f}(\cdot)$ is the estimated probability density function, $f(\cdot)$ is the true probability density function, and $E[\cdot]$ represents the expectation operation. Meanwhile, it is assumed that $\text{MISE}(\cdot)$ holds under weak assumptions

$$\text{MISE}(h) = \text{AMISE}(h) + o\left(\frac{1}{nh} + h^4\right) \quad (13)$$

$$\text{AMISE}(h) = \frac{R(K)}{nh} + \frac{1}{4}m_2(K)^2h^4R(f'') \quad (14)$$

$$R(K) = \int K(x)^2 dx \quad (15)$$

$$m_2(K) = \int x^2 K(x) dx \quad (16)$$

where n is the number of sample data points, h is the bandwidth, AMISE stands for the asymptotic MISE. Minimizing MISE is equivalent to minimizing AMISE, thus setting the derivative of AMISE to 0

$$\frac{\partial}{\partial h} \text{AMISE}(h) = -\frac{R(K)}{nh^2} + m_2(K)^2h^3R(f'') = 0 \quad (17)$$

$$h_{\text{AMISE}} = \frac{R(K)^{\frac{1}{5}}}{m_2(K)^{\frac{2}{5}}R(f'')^{\frac{1}{5}}n^{\frac{1}{5}}} \quad (18)$$

If using Gaussian kernel density estimation, the optimal choice of bandwidth that minimizes the MISE is typically determined to be the following:

$$h = \left(\frac{4\hat{\sigma}^{\frac{1}{5}}}{3n} \right)^{\frac{1}{5}} \approx 1.06\hat{\sigma}n^{-\frac{1}{5}} \quad (19)$$

where $\hat{\sigma}$ represents the sample standard deviation. However, when only the distribution of data points is considered, neglecting their grayscale values, the invalid information from low grayscale values may impact the density estimation results. Therefore, this study integrates both the grayscale and density of the input image, enhancing the probability density image, which is then employed in the computation of the decay rate

$$\begin{aligned} u_i'' &= r_2 \odot u_i' \\ &= F_2(u_i') \odot u_i' \\ &= 0.5u_i' \odot G(T(f_h(u_i') \odot u_i')) + 0.5u_i' \\ &\odot \begin{pmatrix} G(T(f_h(u_i^{11'}) \odot u_i^{11'})) & G(T(f_h(u_i^{12'}) \odot u_i^{12'})) \\ G(T(f_h(u_i^{21'}) \odot u_i^{21'})) & G(T(f_h(u_i^{22'}) \odot u_i^{22'})) \end{pmatrix} \end{aligned} \quad (20)$$

where u_i'' represents the u_i' enhanced through density estimation, r_2 represents the decay rate calculated after density estimation, $u_i^{11'}$, $u_i^{12'}$, $u_i^{21'}$, and $u_i^{22'}$, respectively, represent the four equal parts of upper left, upper right, lower left, and lower right of u_i' .

D. CEOPS Module

In addressing the semantic segmentation challenges posed by random sea conditions, the CEOPS module retains the foundational architecture of feature encoding and decoding. Augmentations are made at the input of the CEOPS module, incorporating spatial attention mechanisms and multiscale convolutions to bolster the model's capacity in processing intricate maritime imagery. This approach facilitates enhanced comprehension of both global contextual structures and local detailed information in the input image and the SCAND module modulation result, thereby fortifying the model's capacity to autonomously discern high-level semantic features. Consequently, the model exhibits improved adaptability to diverse environmental scenarios.

In semantic segmentation tasks of SAR images under random sea conditions, the encoder continuously increases the depth of the network through a hierarchical cascade structure to extract deeper semantic features. However, random sea condition SAR images contain global distributions of random noise and the typical convolution kernel sizes are often set to 3×3 or 5×5 , with a receptive field not exceeding 25 pixels, which may result in a significant proportion of noisy pixels contaminating the receptive field. In addition, aquaculture targets are influenced by complex marine environments, and their scales and shapes may change. The limited receptive field of traditional convolutional layers restricts the model's ability to accurately identify and locate targets. Therefore, the CEOPS module selects dilated convolution as the core for feature extraction to obtain a broader context. Before context interaction, each layer of the network is screened using offset convolution to eliminate the influence of disturbing information as much as possible.

When dealing with complex scenes, one significant reason for the failure of traditional semantic segmentation models is their insufficient capability to handle multiscale information processing and feature interaction. For example, using skip connections may lead to significant noise from the original image being propagated to lower level features, thereby impacting

the accuracy of feature representation. In contrast, the BiFP structure employed in the CEOPS module effectively manages feature information across different levels of the network, facilitating efficient information exchange between feature maps at various levels. This approach aids the model in achieving a more comprehensive understanding of differences between objects and backgrounds, thereby enhancing the model's capability to suppress noise. However, it also results in some loss of fine-grained details of the target object's edges. In addition, CEOPS achieves feature fusion by adaptively selecting feature maps, which, compared to traditional models, such as U-net, can better suppress background noise and adapt to input data under different sea conditions. To restore spatial information in the multidimensional features processed by the BiFP structure, the decoder adopts the combination of upsampling and attention gates. By dynamically adjusting the importance of each feature map, this mechanism directs the model's attention toward aquaculture target regions, mitigating interference from pseudotarget regions generated by random sea conditions.

IV. EXPERIMENTS

The RSC-APMN model proposes two components that require in-depth discussion: the SCAND module and the CEOPS module. To demonstrate the effectiveness of the SCAND module in adaptively enhancing SAR images under random sea conditions, and the capability of the CEOPS module in extracting targets from SAR images in random sea conditions, this article conducted extensive experimental validation. By comprehensively considering key aspects, such as signal-to-noise ratio, preservation rate of target information, and suppression rate of background regions, evaluation metrics tailored to the results of the SCAND module were designed. Subsequently, a hyperparameter comparison experiment is carried out to compare the adaptive enhancement effect of SAR images in sea conditions from 0 to 5, and the experimental results are presented and analyzed. Furthermore, this study validated the effectiveness of the CEOPS module, constructed based on BiFP, in processing SAR images under random sea conditions. Comparative experiments were conducted with unsupervised methods, deep learning models, and the popular CFAR detection algorithm under random sea conditions, further demonstrating the limitations of applying CFAR algorithm theory to semantic segmentation.

All the experiments are implemented in PyTorch 1.7.0, with an Intel Xeon Silver 4210 with 2.40 GHz and an Nvidia GeForce RTX 3080.

A. Dataset

To validate the effectiveness of the RSC-APMN model in extracting information on marine aquaculture under random sea conditions, this study focuses on the marine aquaculture area in Ningde, Fujian, covering the range from $119^\circ \sim 121^\circ\text{E}$ degrees longitude and $26^\circ \sim 28^\circ\text{N}$ degrees latitude across various time frames, and selects the HV polarization SAR data captured by GaoFen-3 satellite, ranging from sea condition levels 0–5 determined according to Table I, captured by GaoFen-3 satellite. The

TABLE I
BEAUFORT WIND LEVELS 0 ~ 6

Level	Wind power	v (m/s)	Wave height (m)
0	Calm	0 ~ 0.2	
1	Light breeze	0.3 ~ 1.5	0.1
2	Light wind	1.6 ~ 3.3	0.2 ~ 0.3
3	Light air	3.4 ~ 5.4	0.6 ~ 1
4	Gentle wind	5.5 ~ 7.9	1 ~ 1.5
5	Moderate wind	8.0 ~ 10.7	2 ~ 2.5
6	Strong wind	10.8 ~ 13.8	3 ~ 4

data are based on ultrafine fringe technology with a resolution of 3 m and a fringe width of 30 km.

The dataset was cropped into images of size 512×512 pixels. Among these, 122 images have been selected for the test set to evaluate the performance of various contrast methods. In addition, 291 images were selected from the dataset as the training set, and 67 images were designated as the validation set, totaling 480 images. Within these 480 images, a subset was specifically chosen to verify the feasibility of the SCAND module for adaptive modulation and enhancement of SAR images under random sea conditions.

B. Evaluation Criteria

Based on the characteristics that the shape structure and backscattering coefficient of aquaculture targets remain higher than ocean background under random sea conditions, using visual interpretation, pixels belonging to the target class were labeled as positive, while all other pixels were labeled as negative. To evaluate the performance of the RSC-APMN model in extracting aquaculture targets under random sea conditions and the ability of the SCAND module to suppress background noise, multiple evaluation indicators are introduced. The primary evaluation metrics [21] include overall accuracy (OA), precision (P), recall (R), $F1$ score, mean intersection over union (MIoU), Kappa coefficient, ICMQ, image contrast (C), target region's decay rate (γ), and nontarget region modulating index (NRMI)

$$\begin{aligned} \text{ICMQ} &= \frac{1}{3}(C + \gamma + \text{NRMI}) \\ C &= \frac{\bar{T}_d - \bar{N}_d}{\bar{T}_d}, \\ \gamma &= \frac{\bar{T}_d}{\bar{T}_o}, \\ \text{NRMI} &= 1 - \frac{10}{m} \sum \left(\frac{N_d}{255} - 0 \right)^2 \end{aligned} \quad (21)$$

where \bar{T}_d and \bar{N}_d represent the mean values of the target region and nontarget region in the modulated image, respectively, \bar{T}_o represents the mean value of the target region in the original image, N_d represents the nontarget region in the modulated image, and m denotes the number of pixels in the nontarget region. Moreover, a larger ICMQ value indicates better results achieved by SCAND.

In binary classification problems, OA refers to the proportion of pixels correctly classified by the model relative to the total

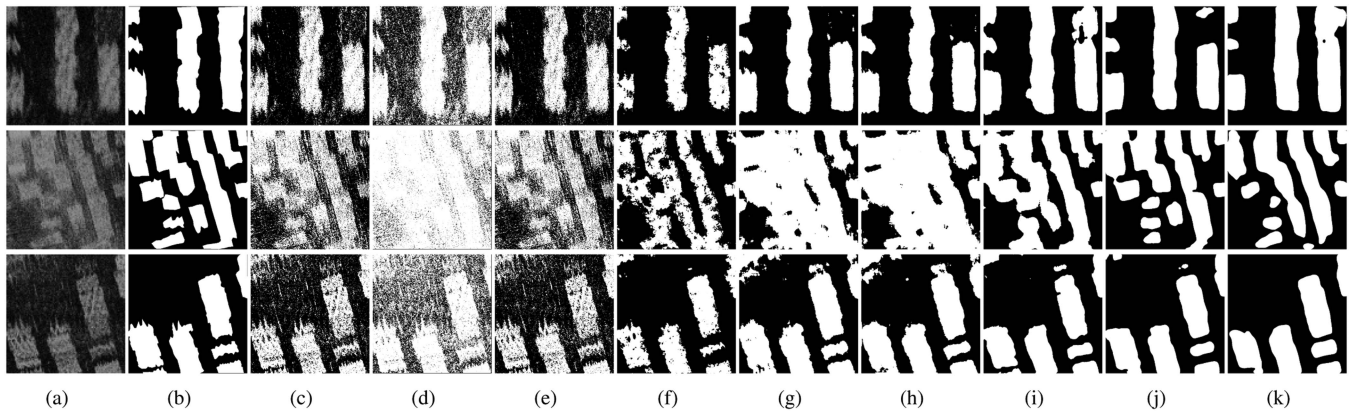


Fig. 6. Experimental results of comparison methods for marine aquaculture under sea condition levels $B3$. (a) Original image. (b) Ground truth. (c) OTSU. (d) 2-D-CFAR. (e) Watershed. (f) SegNet. (g) U-Net. (h) U-Net++. (i) DeepLabv3+. (j) MDOAU-Net. (k) RSC-APMN.

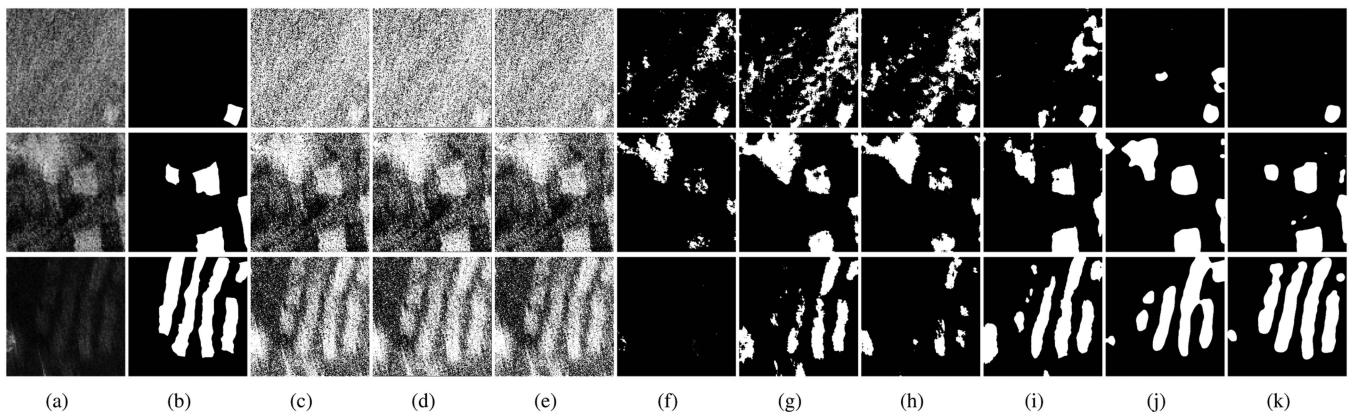


Fig. 7. Experimental results of comparison methods for marine aquaculture under sea condition levels $B4$. (a) Original image. (b) Ground truth. (c) OTSU. (d) 2-D-CFAR. (e) Watershed. (f) SegNet. (g) U-Net. (h) U-Net++. (i) DeepLabv3+. (j) MDOAU-Net. (k) RSC-APMN.

number of pixels. However, in the case of class imbalance, where one class has significantly more samples than the other, accuracy may provide misleading results. MIoU calculates the average ratio of intersection to union for all classes, reflecting the spatial consistency between segmentation results and ground truth labels. The Kappa is a statistical metric used to measure the accuracy of classification models, primarily addressing the limitations of accuracy in situations of class imbalance or random classification, which ranges from -1 to 1 , typically greater than 0 . Specifically, -1 indicates complete inconsistency, 0 indicates chance agreement, and the ranges of 0.0 – 0.20 , 0.21 – 0.40 , 0.41 – 0.60 , 0.61 – 0.80 , and 0.81 – 1 represent levels of agreement categorized as very low, fair, moderate, substantial, and almost perfect, respectively. P emphasizes the proportion of instances predicted as positive that are truly positive, while R emphasizes the proportion of true positive instances successfully captured by the model. The $F1$ score is the harmonic mean of P and recall R , used to evaluate the overall performance of classification models, particularly crucial in scenarios of imbalanced classes. Its values range from 0 to 1 , where a value closer to 1 indicates a better balance between precision and recall, signifying a better

performance in balancing the accuracy of positive class identification and its coverage. ICMQ integrates multiple metrics aiming to comprehensively assess the quality of the result of SCAND module, which includes C , γ , and NRMI. C is used to evaluate image contrast, γ measures the information decay rate in target regions, and NRMI assesses the proximity of nontarget regions to zero value, reflecting the SCAND's effectiveness in noise suppression.

C. Comparative Experiments

In this article, OTSU [44], 2D-CFAR [45], Watershed [46], U-Net [47], SegNet [48], U-Net++[49], DeepLabV3+[50], and MDOAU-Net [51] are compared with the proposed RSC-APMN model. The experimental results of the marine aquaculture under high sea conditions are shown in Figs. 6–8, respectively. Moreover, the corresponding accuracy is tabulated in Tables II–IV, respectively. The best results are marked in bold in the tables.

1) $B3$: Under $B3$ sea condition, as shown in Fig. 6, with the wind field changes, the surface roughness of the sea surface

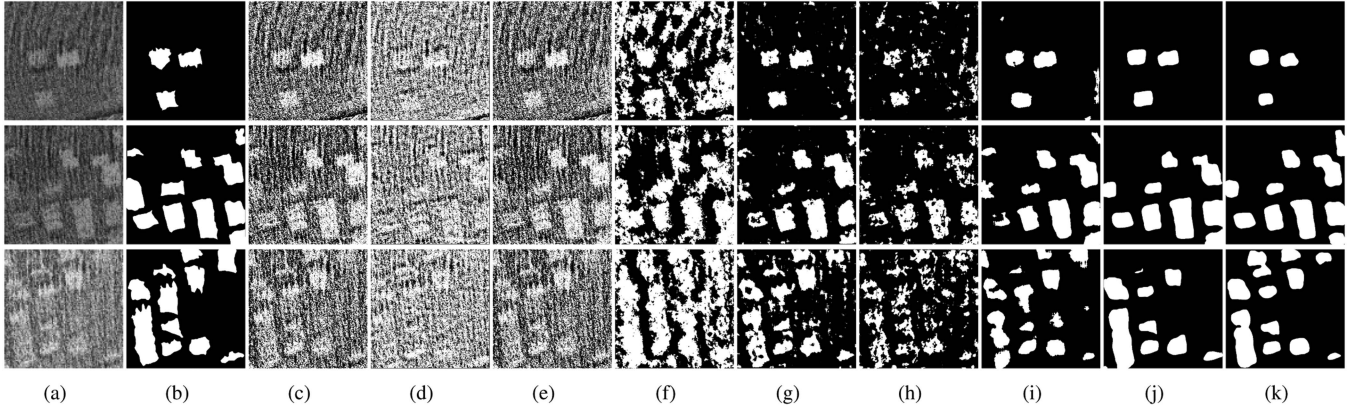


Fig. 8. Experimental results of comparison methods for marine aquaculture under sea condition levels $B5$. (a) Original image. (b) Ground truth. (c) OTSU. (d) 2-D-CFAR. (e) Watershed. (f) SegNet. (g) U-Net. (h) U-Net++. (i) DeepLabv3+. (j) MDOAU-Net. (k) RSC-APMN.

TABLE II
EVALUATION OF COMPARATIVE EXPERIMENTAL RESULTS IN MARINE
AQUACULTURE UNDER $B3$ SEA CONDITIONS

Methods	MIoU	Kappa	OA(%)	P(%)	R(%)	F_1
OTSU [44]	0.627 7	0.607 8	81.35	79.22	75.80	0.770 9
2-D-CFAR [45]	0.498 8	0.326 1	64.52	90.32	52.78	0.664 1
Watershed [46]	0.595 0	0.485 5	74.11	69.13	81.04	0.746 1
SegNet [48]	0.667 2	0.680 0	85.22	72.01	90.53	0.798 0
U-Net [47]	0.711 0	0.661 0	83.25	91.60	77.16	0.827 5
U-Net++ [49]	0.716 6	0.665 0	83.42	92.03	77.52	0.830 9
DeepLabv3+ [50]	0.824 9	0.831 7	91.92	93.26	87.75	0.903 7
MDOAU-Net [51]	0.813 0	0.830 5	92.05	87.18	92.30	0.896 2
RSC-APMN	0.821 1	0.834 1	92.11	89.80	90.57	0.901 3

TABLE III
EVALUATION OF COMPARATIVE EXPERIMENTAL RESULTS IN MARINE
AQUACULTURE UNDER $B4$ SEA CONDITIONS

Methods	MIoU	Kappa	OA(%)	P(%)	R(%)	F_1
OTSU [44]	0.195 2	0.141 3	50.76	80.71	21.63	0.303 3
2-D-CFAR [45]	0.191 5	0.136 3	53.24	76.11	21.44	0.298 4
Watershed [46]	0.365 2	0.242 6	61.06	41.82	74.20	0.535 0
SegNet [48]	0.104 5	0.143 6	80.12	31.82	21.41	0.180 2
U-Net [47]	0.298 0	0.360 9	80.81	70.54	44.06	0.436 7
U-Net++ [49]	0.177 3	0.227 1	78.53	53.74	41.34	0.293 3
DeepLabv3+ [50]	0.451 8	0.539 4	87.08	78.58	55.50	0.596 3
MDOAU-Net [51]	0.505 7	0.615 7	87.58	79.55	61.66	0.666 8
RSC-APMN	0.743 3	0.816 9	91.87	83.28	84.60	0.836 7

TABLE IV
EVALUATION OF COMPARATIVE EXPERIMENTAL RESULTS IN MARINE
AQUACULTURE UNDER $B5$ SEA CONDITIONS

Methods	MIoU	Kappa	OA(%)	P(%)	R(%)	F_1
OTSU [44]	0.262 4	0.183 9	58.66	76.43	29.29	0.401 8
2-D-CFAR [45]	0.214 0	0.063 5	42.46	79.95	23.04	0.341 6
Watershed [46]	0.322 0	0.198 4	58.54	36.63	72.71	0.487 2
SegNet [48]	0.341 2	0.317 5	65.53	84.09	37.01	0.485 0
U-Net [47]	0.613 3	0.701 9	83.20	75.69	77.33	0.758 7
U-Net++ [49]	0.429 2	0.509 5	83.34	56.96	64.94	0.593 4
DeepLabv3+ [50]	0.642 0	0.729 7	85.87	71.67	86.57	0.780 7
MDOAU-Net [51]	0.655 2	0.7722	86.83	73.85	91.85	0.817 6
RSC-APMN	0.771 5	0.775 2	92.14	77.99	92.62	0.846 8

gradually increases, leading to a transition in the reflection characteristics from quasispecular to diffuse reflection, and the backscattering coefficient gradually increases. In SAR imaging, due to the overlapping effects of scattering targets within the resolution cell, the signal-to-noise ratio of the image begins to decrease, resulting in an increase in image blur. In addition, there

is a probability of wind-induced surface waves, resulting in slight light and dark streaks on SAR images. However, compared to higher sea conditions, such interference is relatively minor, with a small impact on image quality and target shape structure.

Compared to deep learning, OTSU, 2-D-CFAR, and Watershed are more susceptible to speckle noise and background noise. Nonetheless, in $B3$ sea conditions, unsupervised methods based on pixel values can predict object boundaries and positions relatively accurately. This capability arises from the distinct grayscale distributions between targets and backgrounds typically observed in low sea condition scenarios, allowing unsupervised methods to effectively segment the image into foreground and background using thresholding. This indicates that these methods demonstrate a certain level of feature extraction capability under low sea conditions. However, these approaches overlook the semantic information of the targets, resulting in lower Kappa coefficients and MIoU scores. In addition, the performance of 2-D-CFAR is constrained by the size of the detection window. In the case of rich targets, 2-D-CFAR can effectively set thresholds for the target and background. However, sparse target scenarios may result in unstable classification outcomes due to limited consideration of global image features.

When compared with the deep learning method, in $B3$ sea condition, the semantic segmentation performance of each model did not decrease significantly, as shown in Table II, the average test values of OA, F_1 , and Kappa remained at a high level. In addition to processing images with minor background noise interference or adhesion between some objects, SegNet showed some missing detection. This is because SegNet retained the position information of the maximum pooling layer for up-sampling. At the same time, U-Net and U-Net ++ showed a certain adhesion phenomenon to the aquaculture targets. This may be due to the fact that the idea of jumping connections fails to effectively integrate feature information from different scales and different levels, making it difficult for the network to distinguish small differences between targets. DeepLabV3+ and MDOAU-Net demonstrate more stable and superior performance in semantic segmentation tasks. They both utilize dilated convolutions to better capture contextual information

and multiscale features of the targets. DeepLabV3+ further enhances the restoration of target details and boundaries during the decoding stage by introducing the atrous spatial pyramid pooling (ASPP) module. Meanwhile, MDOA-UNet improves segmentation effectiveness by employing offset convolutions to filter out irrelevant features. The RSC-APMN integrates the advantages of both DeepLabV3+ and MDOA-UNet, utilizing BiFP instead of ASPP to enhance feature fusion capability, maintaining high levels of performance in terms of OA, MIOU, and Kappa metrics.

2) *B4*: When the sea condition level reaches *B4*, as shown in Fig. 7, the roughness of the sea surface significantly increases, leading to random scattering of electromagnetic waves in all directions and exacerbating the phenomenon of diffuse reflection on the sea surface. This phenomenon results in a significant enhancement of background clutter signals, causing the target signals to become blurred or confused, thereby weakening the intensity of target signals in the image, reducing the contrast between targets and backgrounds, and increasing the difficulty of target detection and recognition.

In such scenario, pixel-value-based methods, such as OTSU, 2-D-CFAR, and Watershed, which lack semantic understanding, fail completely. The OTSU operates by finding the grayscale threshold that maximizes interclass variance, suitable for images with clearly distinct target and background grayscale distributions, characterized by bimodal histograms. However, in the *B4* sea condition, pixel distributions are influenced by diffuse reflection, resulting in a more uniform distribution compared to *B3*. This makes it challenging to accurately determine effective thresholds. Similarly, the 2-D-CFAR adjusts thresholds dynamically by adapting detection windows. However, in scenarios where the target is sparse and the image contrast is reduced, as is typical of *B4* sea conditions, unstable threshold selections can result in a high number of false alarms and missed detections. In addition, in diffuse reflection imagery, where targets and background grayscale values are similar, this algorithm struggles to effectively differentiate between them. Meanwhile, Watershed algorithms are typically employed for segmenting objects with well-defined boundaries. Nevertheless, in diffuse reflection imagery, the boundaries of targets may lack clarity or blend into surrounding backgrounds, potentially leading to issues of oversegmentation.

SAR images formed in such sea conditions are relatively difficult to distinguish in *B0–B5* sea conditions, the strong background noise directly impairs the performance of deep learning models and imposes higher demands on their semantic understanding capabilities. Therefore, under *B4* sea conditions, the deficiencies previously noted in SegNet, U-Net, and U-Net++ during *B3* conditions become more pronounced. As shown in Fig. 7, MDOAU-net, limited by the structure of the jump connection, significantly interfered with noise and attenuation of target signal strength, resulting in a large number of errors. Although Deeplabv3+ exhibits slightly better performance due to its ASPP structure advantage, it also begins to exhibit a certain number of errors. Overall, traditional semantic segmentation methods have not adequately accounted for the effects of environmental changes on model performance. When confronted with complex

environments, such as random sea conditions, background noise significantly reduces various performance metrics. Despite the OA still being maintained at over 80%, metrics such as MIOU, Kappa, *P*, *R*, and *F1* decreased by approximately 20%–30%, indicating significant confusion or omission. However, the RSC-APMN effectively alleviates performance degradation in random sea conditions, showcasing strong noise suppression and semantic comprehension capabilities in blurry and target-confused SAR images.

3) *B5*: When the sea condition reaches *B5*, as shown in Fig. 8, the random sea surface is formed by the combination of waves of both sizes, and the small-scale wave equivalent to the wavelength of the electromagnetic wave is superimposed on the large-scale wave. The scattering in small areas is primarily caused by small-scale waves, while long waves modulate the local incidence angle of electromagnetic waves through their tilted wavefronts, thereby affecting the radar's backscatter cross-section. At this point, the primary echo mechanism of electromagnetic waves is the Bragg scattering caused by the periodic structure of the target surface, resulting in alternating bright and dark stripes in SAR images. Typically, compared to the diffuse reflection in *B3* sea conditions, target features under this reflection background are more easily highlighted or identified. However, as the sea condition level increases, factors such as sea foam, mist, and rainfall may affect the extraction of SAR sea surface information.

In the *B5* sea condition, the boundary and gray difference between the target and the background are usually more obvious than *B4*, but they are affected by the globally distributed light and dark striped noise. The gray value of this fringe noise is very close to the target, and the floating raft target is often submerged in it. Because unsupervised methods, such as OTSU, 2-D-CFAR, and Watershed, lack adequate semantic information understanding, they often misidentify these noisy areas as targets, resulting in extremely poor performance of all evaluation indicators. Furthermore, in deep learning approaches, Segnet may misclassify substantial globally distributed bright striped noise as targets due to limitations from max-pooling and lack of spatial and semantic interaction, which is reflected in its OA and *R*. Although U-Net and U-Net++ enhance model performance by boosting information transfer among different-level feature maps, limitations in information transmission result in errors when handling target edges and multiscale targets. MOAU-Net and Deeplabv3+ exhibit higher stability in *B5* sea condition environments dominated by Bragg scattering, owing to their capabilities in multiscale information integration, feature selection, and multidimensional feature fusion.

In summary, unsupervised methods struggle with SAR imagery due to significant variations in surface scattering characteristics across different sea conditions. This makes it challenging to identify a universally applicable image feature for threshold segmentation. Moreover, classical deep learning methods have not effectively utilized environmental information and lack robust feature exploration and interaction capabilities in complex scenarios, resulting in significant performance degradation in random sea conditions. Through in-depth analysis of the strengths and weaknesses of various deep learning models under

sea conditions ranging from $B3$ to $B5$, this study improves upon the well-performing MDOAU-Net and DeepLabV3+ models under random sea conditions to design the RSC-APMN. This network is capable of adaptively suppressing background noise according to sea condition levels while possessing strong capabilities for multidimensional feature information propagation and fusion. Consequently, it effectively mitigates the significant performance degradation caused by variations in SAR image target and background features due to changes in marine environments, as shown in Fig. 9, resulting in the best comprehensive performance across all sea conditions.

D. Hyperparameter and Ablation Part

The exponent n of the SCAND module decay ratio is a key hyperparameter, as shown in equation (11), discussed in this article, utilized to suppress background noise in the random sea conditions. The discussion emphasizes the necessity of considering various sea condition levels when setting n . Setting it too high can lead to a significant loss of target information, while setting it too low may not effectively suppress ocean noise. During the experimental phase, n was varied from 0 to 5 for comparison purposes, assessing the performance of each adjustment in both suppressing ocean noise and retaining valuable information, which aimed to determine the most suitable n value adaptable to different sea conditions. The experimentation on hyperparameters is designed to introduce the ICMQ metric, aiming to comprehensively evaluate the performance of the SCAND module.

With the modulation coefficient n increases, as shown in Fig. 10, the background noise is modulated by the SCAND module. At a smaller n value, the loss of information in the target area is minimal, resulting in a significant improvement in image contrast and a substantial increase in the ICMQ. However, once n exceeds a certain threshold, the information within the target area begins to decay because the background noise has been reduced to extremely low levels, resulting in a decline in the ICMQ. Therefore, in a variety of sea conditions, it is crucial to choose the best n value corresponding to ICMQ. At the same time, the comprehensive quality of the $B3$ sea condition image is the best without SCAND modulation. In the $B5$ sea condition, due to the influence of sea surface Bragg scattering, there is a lot of fringe noise in the image, which leads to the decrease of ICMQ value. In $B4$ sea condition, the image is seriously affected by diffuse reflection, resulting in the worst image contrast and the lowest ICMQ value, which is fully consistent with the analysis of each sea condition image in the comparison experiment, indicating the effectiveness of ICMQ design. Therefore, in the case of $B3$ sea condition, to avoid the loss of critical information, $n = 0.6$ is considered to be the most suitable hyperparameter. Under the $B4$ sea condition, to balance the clutter suppression caused by diffuse reflection and the preservation of target information, $n = 2.8$ can obtain the optimal ICMQ value. Under the $B5$ sea condition, adopting $n = 1.8$ can effectively remove the fringe noise from the background.

Figs. 11 and 12 present partial results of the module's grayscale intensity estimation and density estimation under high

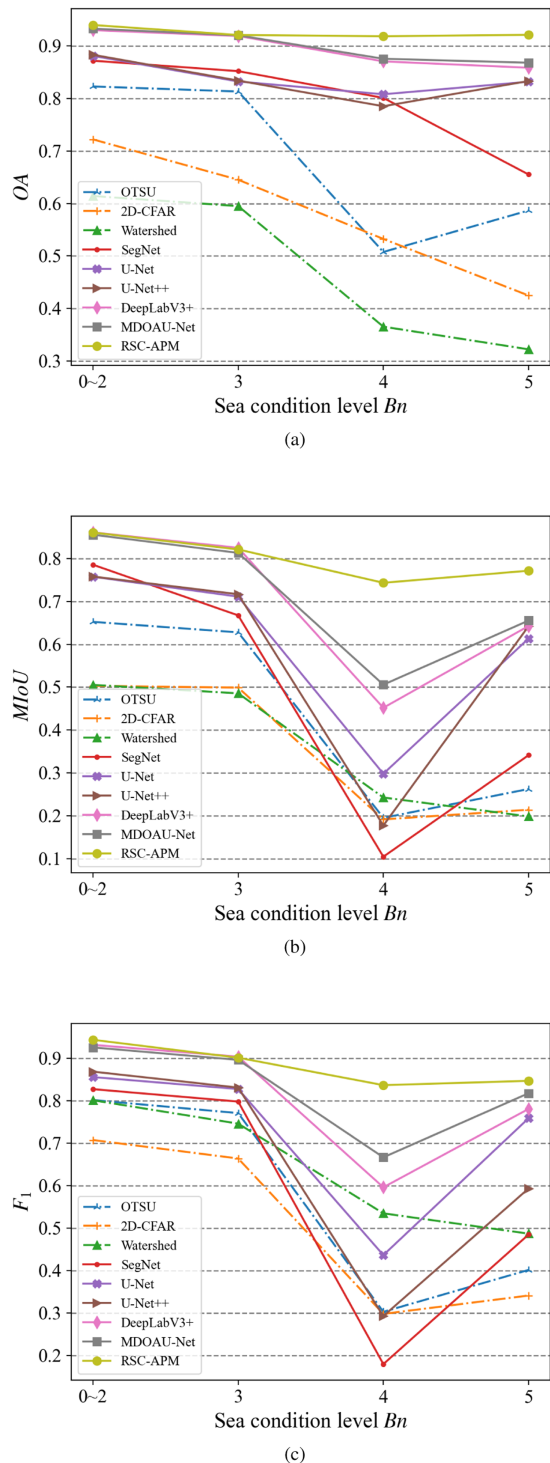


Fig. 9. Impact of different sea condition levels on unsupervised methods and deep learning approaches. (a) OA. (b) MIOU. (c) $F1$.

sea conditions, depicting the effects as n values increase. It is observed that upon selecting an appropriate n value, the grayscale density estimation under high sea conditions effectively eliminates a significant portion of nontarget noise while preventing substantial loss of target information. However, despite the grayscale density estimation, residual scattered noise

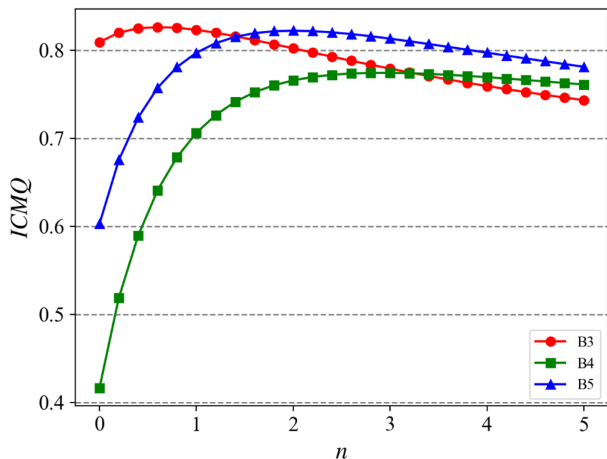


Fig. 10. Experiment on the comprehensive modulating effect of different n for $B3$ – $B5$ sea condition images.

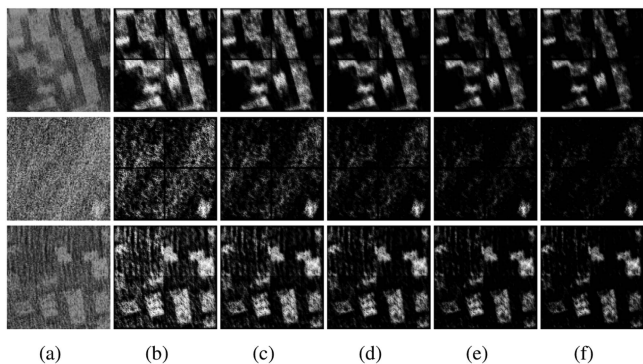


Fig. 11. Partial experimental results of grayscale intensity estimation under different hyperparameter values of n . (a) Original image. (b) $n = 0.6$. (c) $n = 1.8$. (d) $n = 2.8$. (e) $n = 4$. (f) $n = 5$.

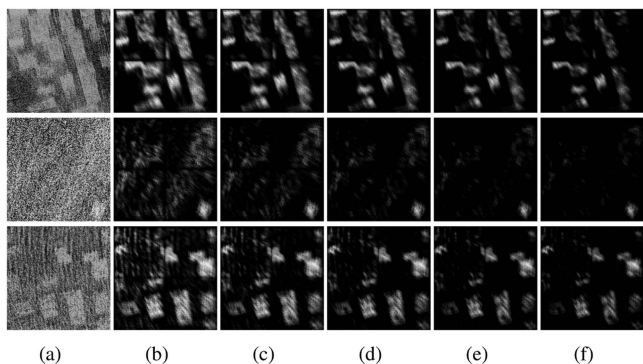


Fig. 12. Partial experimental results of density estimation under different hyperparameter values of n . (a) Original image. (b) $n = 0.6$. (c) $n = 1.8$. (d) $n = 2.8$. (e) $n = 4$. (f) $n = 5$.

may still interfere with subsequent information extraction. However, Fig. 12 demonstrates that employing density estimation for further denoising improves image quality.

Under the same hyperparameter settings, as shown in Table V, the study conducted ablation experiments to investigate the effects of the SCLA module and SCAND module on the

TABLE V
RESULTS OF THE ABLATION EXPERIMENTS

SCLA module	APM module	MIoU	OA(%)
		0.707 6	83.32
	✓	0.745 3	88.35
✓	✓	0.778 6	92.04

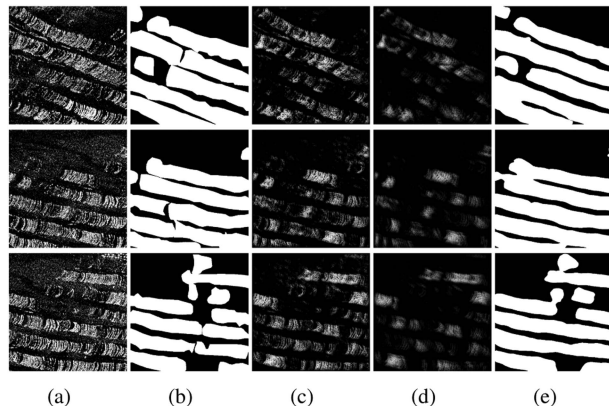


Fig. 13. Experimental results of regional verification. (a) Original image. (b) Ground truth. (c) Grayscale intensity estimation of SCAND. (d) Density estimation of SCAND. (e) RSC-APMN.

RSC-APMN model. Disregarding the SCLA module implies testing the RSC-APMN without considering changes in sea condition levels. In addition, ignoring the SCAND module means not modulating SAR images for background noise suppression and other enhancements but directly testing the RSC-APMN. It is important to note that the CEOPS module, proposed in this article for semantic segmentation under stochastic sea conditions, cannot undergo ablation experiments.

E. Validation of Different Regional Applicability

To further validate the efficacy of the method, another segmentation experiment is conducted, which is located in Changhai, Dalian, Liaoning. The SAR image was captured at geographical coordinates, 39°N , 122°E on 17 June 2021, at 17:48, under sea condition $B3$. According to the results shown in Fig. 13, the RSC-APM model effectively integrates significant features from both the original image and SCAND modulation outcomes, achieving more comprehensive information utilization. The evaluation reveals that the RSC-APM model achieves an MIoU of 0.8574, a Kappa of 0.7455, an OA of 91.27%, and an $F1$ score reaching 92.33% on the dataset of this region. Hence, even across regions with varying aquaculture characteristics, the model demonstrates outstanding performance in information extraction and exhibits significant generalization capabilities.

F. Extraction Experiment in a Single Image Under Varying Wind Speeds

When analyzing SAR images under random sea conditions, the same image may contain multiple different sea condition scenes. Furthermore, images with similar environmental information may also exhibit different characteristics, which are

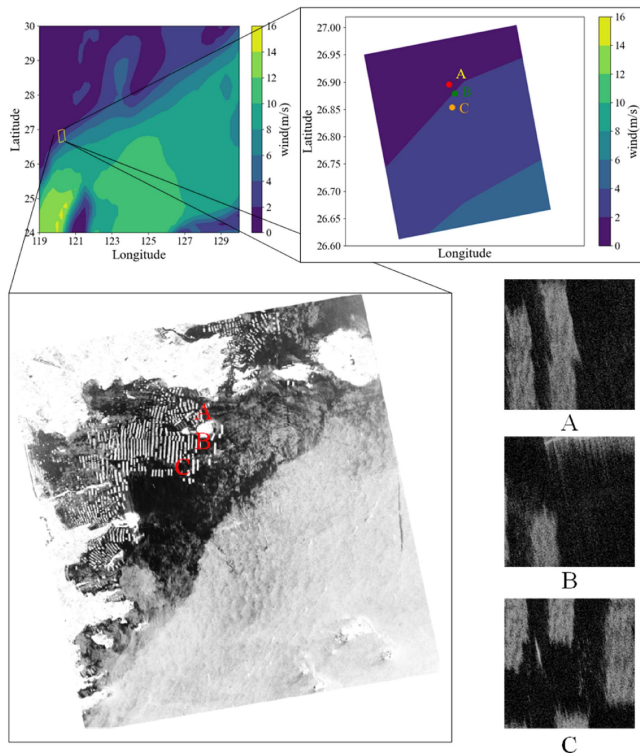


Fig. 14. Visual representation of sea surface wind speed captured at latitude $24^{\circ} \sim 30^{\circ}\text{N}$ and longitude $119^{\circ} \sim 130^{\circ}\text{E}$ at 10:05 on 16 May 2022. Areas with varying wind speed information were selected for the validation experiments.

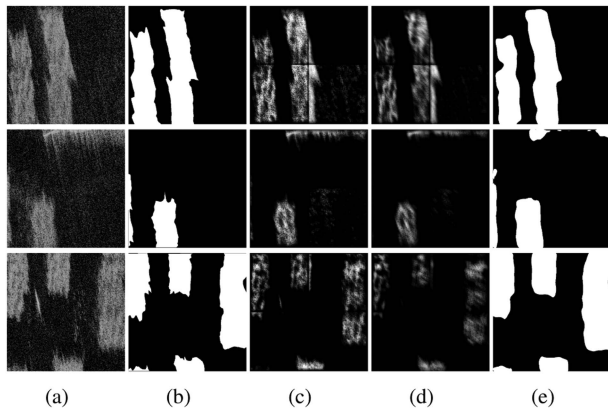


Fig. 15. Comparative experiment of images with uniform wind speed information. (a) Original image. (b) Ground truth. (c) Grayscale intensity estimation of SCAND. (d) Density estimation of SCAND. (e) RSC-APMN.

caused by other factors, such as satellite imaging conditions and seabed terrain. The SCAND module of RSC-APMN not only considers the levels of sea condition, but also considers the signal-to-noise characteristics of the image to calculate the decay rate. To validate the stability of the SCAND module in processing such images, three regions within the same SAR image exhibiting varying wind speed information were selected for experimental verification.

As shown in Figs. 14 and 15, when disparate wind speed data is present within a single image, the SCAND module

TABLE VI
EVALUATION OF COMPARATIVE EXPERIMENTAL RESULTS OF IMAGES WITH UNIFORM WIND SPEED.

Areas	MIoU	Kappa	OA(%)	P(%)	R(%)	F_1
Area A	0.910 8	0.931 5	97.03	97.34	93.41	0.953 3
Area B	0.781 8	0.779 5	95.76	70.19	97.47	0.802 4
Area C	0.893 0	0.910 6	95.84	90.00	98.11	0.939 5

modulates the decay ratios in accordance with the specific wind speed information pertaining to each region. Moreover, even when factors result in disparate image characteristics despite identical environmental conditions, the SCAND module also can enhance SAR images based on its inherent signal-to-noise ratio characteristics, thereby reducing noise interference in the background. RSC-APMN can further process the feature-enhanced results from the SCAND module to better leverage semantic information in the image, thereby improving overall segmentation quality and accuracy. As shown in Table VI, the model maintains stable extraction accuracy, with the OA surpassing 95%, while the F_1 remains consistently above 0.80. RSC-APMN demonstrates excellent adaptability in handling images with different imaging characteristics and uneven background distributions, even under the influence of environmental precision.

V. CONCLUSION

This article proposes an RSC-APMN model aimed at mitigating the significant impact of oceanic conditions on SAR image quality and information extraction accuracy. Tailored to the characteristics of SAR images under random sea conditions, the network achieves adaptive enhancement of SAR images based on sea condition levels by designing the SCLA module and SCAND module. This effectively suppresses the strong clutter background noise caused by sea conditions while maximizing the retention of critical information in target areas, thereby enhancing image contrast. To address the significant decrease in the accuracy of semantic segmentation models in complex and changing marine environments, the CEOPS module is designed. This module facilitates the interaction and fusion of multilevel semantic information without introducing a large number of additional parameters, thereby improving the adaptability and robustness of the model to complex and changing scenes. The experimental data encompasses a range of sea conditions, from B_0 to B_5 , and includes a detailed analysis of environmental factors influencing sea surface scattering characteristics and the imaging features of SAR images under random sea conditions. By comparing the performance of the RSC-APMN with that of current unsupervised methods and deep learning models applicable to random sea condition target extraction, the superiority of the RSC-APMN in extracting information from aquaculture under random sea conditions is validated.

REFERENCES

- [1] H. K. Alleyway, C. L. Gillies, M. J. Bishop, R. R. Gentry, S. J. Theuerkauf, and R. Jones, "The ecosystem services of marine aquaculture: Valuing benefits to people and nature," *BioScience*, vol. 69, no. 1, pp. 59–68, 2019.

- [2] X. Liu et al., "Mapping China's offshore mariculture based on dense time-series optical and radar data," *Int. J. Digit. Earth*, vol. 15, no. 1, pp. 1326–1349, 2022.
- [3] L. Falconer et al., "Planning and licensing for marine aquaculture," *Rev. Aquaculture*, vol. 15, no. 4, pp. 1374–1404, 2023.
- [4] J. Wang, A. H. Beusen, X. Liu, and A. F. Bouwman, "Aquaculture production is a large, spatially concentrated source of nutrients in Chinese freshwater and coastal seas," *Environ. Sci. Technol.*, vol. 54, no. 3, pp. 1464–1474, 2019.
- [5] Y. Duan et al., "Tracking changes in aquaculture ponds on the China coast using 30 years of landsat images," *Int. J. Appl. Earth Observ. Geoinf.*, vol. 102, 2021, Art. no. 102383.
- [6] T. Fu, L. Zhang, X. Yuan, B. Chen, and M. Yan, "Spatio-temporal patterns and sustainable development of coastal aquaculture in Hainan Island, China: 30 years of evidence from remote sensing," *Ocean Coastal Manage.*, vol. 214, 2021, Art. no. 105897.
- [7] M. Lin and Y. Jia, "Past, present and future marine microwave satellite missions in China," *Remote Sens.*, vol. 14, no. 6, 2022, Art. no. 1330.
- [8] T. Hou, W. Sun, C. Chen, G. Yang, X. Meng, and J. Peng, "Marine floating raft aquaculture extraction of hyperspectral remote sensing images based decision tree algorithm," *Int. J. Appl. Earth Observ. Geoinf.*, vol. 111, 2022, Art. no. 102846.
- [9] J. Wang, X. Yang, Z. Wang, D. Ge, and J. Kang, "Monitoring marine aquaculture and implications for marine spatial planning—an example from Shandong Province, China," *Remote Sens.*, vol. 14, no. 3, 2022, Art. no. 732.
- [10] X. Zhang, J. Xu, Y. Chen, K. Xu, and D. Wang, "Coastal wetland classification with GF-3 polarimetric SAR imagery by using object-oriented random forest algorithm," *Sensors*, vol. 21, no. 10, 2021, Art. no. 3395.
- [11] F. Bovenga, "Special issue "synthetic aperture radar (SAR) techniques and applications,"" *Sensors*, vol. 20, no. 7, 2020, Art. no. 1851.
- [12] B. Chu, Y. Chen, Y. Zhang, G. Zhang, X. Xiang, and X. Zhang, "Numerical study on wave-induced hydro-elastic responses of a floating raft for aquaculture," *Ocean Eng.*, vol. 240, 2021, Art. no. 109869.
- [13] L. Gansel, F. Oppedal, J. Birkevold, and S. Tuene, "Drag forces and deformation of aquaculture cages—full-scale towing tests in the field," *Aquacultural Eng.*, vol. 81, pp. 46–56, 2018.
- [14] J. Liu, Y. Lu, X. Guo, and W. Ke, "A deep learning method for offshore raft aquaculture extraction based on medium resolution remote sensing images," *IEEE J. Sel. Topics Appl. Earth Observ. Remote Sens.*, vol. 16, pp. 6296–6309, 2023.
- [15] B. Cui, D. Fei, G. Shao, Y. Lu, and J. Chu, "Extracting raft aquaculture areas from remote sensing images via an improved U-Net with a PSE structure," *Remote Sens.*, vol. 11, no. 17, 2019, Art. no. 2053.
- [16] Y. Zhang et al., "Combining segmentation network and nonsubsampling contourlet transform for automatic marine raft aquaculture area extraction from Sentinel-1 images," *Remote Sens.*, vol. 12, no. 24, 2020, Art. no. 4182.
- [17] H. Su, S. Wei, J. Qiu, and W. Wu, "RaftNet: A new deep neural network for coastal raft aquaculture extraction from landsat 8 OLI data," *Remote Sens.*, vol. 14, no. 18, 2022, Art. no. 4587.
- [18] J. Zhou, C. Chu, G. Zhou, X. Wang, K. Wang, and J. Fan, "Unsupervised segmentation of cage aquaculture in SAR images based on invariant information," in *Proc. 2022 14th Int. Conf. Adv. Comput. Intell. (ICACI)*. IEEE, 2022, pp. 212–215.
- [19] J. Fan, J. Zhou, X. Wang, and J. Wang, "A self-supervised transformer with feature fusion for SAR image semantic segmentation in marine aquaculture monitoring," *IEEE Trans. Geosci. Remote Sens.*, vol. 61, 2023, Art. no. 4207915.
- [20] J. Fan, X. Wang, X. Wang, X. Liu, J. Zhao, and Q. Meng, "GF-3 PolSAR marine aquaculture recognition based on complex convolutional neural networks," in *Proc. 2019 10th Int. Conf. Intell. Control Inf. Process. (ICICIP)*. IEEE, 2019, pp. 112–115.
- [21] X. Wang, J. Zhou, and J. Fan, "IDUDL: Incremental double unsupervised deep learning model for marine aquaculture SAR images segmentation," *IEEE Trans. Geosci. Remote Sens.*, vol. 60, 2022, Art. no. 4209412.
- [22] J. Zhou, M. Li, X. Wang, and J. Fan, "Unsupervised mutual information and superpixel constraints in SAR marine aquaculture extraction," in *Proc. 2023 15th Int. Conf. Adv. Comput. Intell. (ICACI)*. IEEE, 2023, pp. 1–5.
- [23] Y. Hou, X. Jiang, and Y. Liu, "China coastal seas under severe sea state: Remote sensing and dynamics studies," *Chin. J. Oceanol. Limnol.*, vol. 33, no. 5, 2015, Art. no. 1101.
- [24] Z. Sun et al., "Contribution of breaking wave on the co-polarized backscattering measured by the Chinese Gaofen-3 SAR," *Int. J. Remote Sens.*, vol. 43, no. 4, pp. 1384–1408, 2022.
- [25] Y. Du et al., "Effects of temperature on sea surface radar backscattering under neutral and nonneutral atmospheric conditions for wind retrieval applications: A numerical study," *IEEE Trans. Geosci. Remote Sens.*, vol. 59, no. 4, pp. 2727–2743, Apr. 2021.
- [26] W. Shao, Y. Zhou, Q. Zhang, and X. Jiang, "Machine learning-based wind direction retrieval from quad-polarized Gaofen-3 SAR images," *IEEE J. Sel. Topics Appl. Earth Observ. Remote Sens.*, vol. 17, pp. 808–816, 2024.
- [27] X. Zhang, X. Su, and Z. Wu, "Composite backscatter characteristics of conductive/dielectric ships and sea surfaces with breaking waves under high sea conditions," *Sensors*, vol. 23, no. 10, 2023, Art. no. 4904.
- [28] W. Jiang, L. Wang, X. Li, G. Liu, and M. Zhang, "Simulation of a wideband radar echo of a target on a dynamic sea surface," *Remote Sens.*, vol. 13, no. 16, 2021, Art. no. 3186.
- [29] N. Jiao, F. Wang, H. You, J. Liu, and X. Qiu, "A generic framework for improving the geopositioning accuracy of multi-source optical and SAR imagery," *ISPRS J. Photogrammetry Remote Sens.*, vol. 169, pp. 377–388, 2020.
- [30] M. di Bisceglie and C. Galdi, "CFAR detection of extended objects in high-resolution SAR images," *IEEE Trans. Geosci. Remote Sens.*, vol. 43, no. 4, pp. 833–843, Apr. 2005.
- [31] X. Qin, S. Zhou, H. Zou, and G. Gao, "A CFAR detection algorithm for generalized gamma distributed background in high-resolution SAR images," *IEEE Geosci. Remote Sens. Lett.*, vol. 10, no. 4, pp. 806–810, Jul. 2013.
- [32] G. Gao and G. Shi, "CFAR ship detection in nonhomogeneous sea clutter using polarimetric SAR data based on the notch filter," *IEEE Trans. Geosci. Remote Sens.*, vol. 55, no. 8, pp. 4811–4824, Aug. 2017.
- [33] Y. Yang, S.-P. Xiao, and X.-S. Wang, "Radar detection of small target in sea clutter using orthogonal projection," *IEEE Geosci. Remote Sens. Lett.*, vol. 16, no. 3, pp. 382–386, Mar. 2019.
- [34] J. Ai, Q. Luo, X. Yang, Z. Yin, and H. Xu, "Outliers-robust CFAR detector of gaussian clutter based on the truncated-maximum-likelihood-estimator in SAR imagery," *IEEE Trans. Intell. Transp. Syst.*, vol. 21, no. 5, pp. 2039–2049, May 2020.
- [35] J. Xie and X. Xu, "Phase-feature-based detection of small targets in sea clutter," *IEEE Geosci. Remote Sens. Lett.*, vol. 19, 2022, Art. no. 3507405.
- [36] Y. Fan, D. Chen, M. Tao, J. Su, and L. Wang, "Parameter estimation for sea clutter pareto distribution model based on variable interval," *Remote Sens.*, vol. 14, no. 10, 2022, Art. no. 2326.
- [37] Z. Xie, Y. Cheng, H. Wu, L. Zhang, and H. Wang, "Ship target detection in SAR imagery based on maximum eigenvalue detector," *IEEE Geosci. Remote Sens. Lett.*, vol. 19, 2022, Art. no. 4513605.
- [38] Y. Wang, W. Zhao, X. Wang, J. Chen, H. Li, and G. Cui, "Nonhomogeneous sea clutter suppression using complex-valued U-Net model," *IEEE Geosci. Remote Sens. Lett.*, vol. 19, 2022, Art. no. 4027705.
- [39] J. Wang and S. Li, "Maritime radar target detection in sea clutter based on CNN with dual-perspective attention," *IEEE Geosci. Remote Sens. Lett.*, vol. 20, 2023, Art. no. 3500405.
- [40] Q. Fan et al., "Ship detection using a fully convolutional network with compact polarimetric SAR images," *Remote Sens.*, vol. 11, no. 18, 2019, Art. no. 2171.
- [41] M. Tan, R. Pang, and Q. Le, "EfficientDet: Scalable and efficient object detection," in *Proc. IEEE/CVF Conf. Comput. Vis. Pattern Recognit.*, 2020, pp. 10778–10787.
- [42] S. Woo, J. Park, J. Lee, and I. S. Kweon, "CBAM: Convolutional block attention module," in *Proc. Eur. Conf. Comput. Vis. (ECCV)*, 2018, pp. 3–19.
- [43] R. Alcock and D. Morgan, "Investigations of wind and sea state with respect to the beaufort scale," *Weather*, vol. 33, no. 7, pp. 271–277, 1978.
- [44] N. Otsu, "A threshold selection method from gray-level histograms," *IEEE Trans. Syst., Man, Cybern.*, vol. 9, no. 1, pp. 62–66, Jan. 1979.
- [45] M. Kronauge and H. Rohling, "Fast two-dimensional CFAR procedure," *IEEE Trans. Aerosp. Electron. Syst.*, vol. 49, no. 3, pp. 1817–1823, Jul. 2013.
- [46] A. S. Kornilov and I. V. Safonov, "An overview of watershed algorithm implementations in open source libraries," *J. Imag.*, vol. 4, no. 10, 2018, Art. no. 123.
- [47] O. Ronneberger, P. Fischer, and T. Brox, "U-Net: Convolutional networks for biomedical image segmentation," in *Med. Image Comput. Comput.-Assist. Interv.*, 2015, pp. 234–241.
- [48] V. Badrinarayanan, A. Kendall, and R. Cipolla, "SegNet: A deep convolutional encoder-decoder architecture for image segmentation," *IEEE Trans. Pattern Anal. Mach. Intell.*, vol. 39, no. 12, pp. 2481–2495, Dec. 2017.

- [49] Z. Zhou, M. M. Rahman Siddiquee, N. Tajbakhsh, and J. Liang, "UNet: A nested U-Net architecture for medical image segmentation," in *Deep Learn. Med. Image Anal. Multimodal Learn. Clin. Decis. Support: 4th Int. Workshop, DLMIA 2018, 8th Int. Workshop, ML-CDS 2018, Held Conjunction with MICCAI 2018*, Granada, Spain, Sep. 20, 2018, Proceedings 4. Springer, 2018, pp. 3–11.
- [50] L. Chen, Y. Zhu, G. Papandreou, F. Schroff, and H. Adam, "Encoder-decoder with atrous separable convolution for semantic image segmentation," in *Proc. Eur. Conf. Comput. Vis. (ECCV)*, 2018, pp. 801–818.
- [51] J. Wang, J. Fan, and J. Wang, "MDOAU-Net: A lightweight and robust deep learning model for SAR image segmentation in aquaculture raft monitoring," *IEEE Geosci. Remote Sens. Lett.*, vol. 19, 2022, Art. no. 4504505.



Qiweng Deng received the B.S. degree in automatic from Dalian Polytechnic University, Dalian, China, in 2022. He is currently working toward the M.S. degree in control engineering from the School of Control Science and Engineering, Dalian University of Technology, Dalian, China.

His research interests include deep learning and high sea condition remote sensing image processing.



Jianchao Fan (Member IEEE) received the B.S. degree in automatic technology and Ph.D. degrees in control science and control engineering from the School of Control Science and Engineering, Dalian University of Technology, Dalian, China, in 2007 and 2012, respectively.

From 2013 to 2016, he was a Postdoctoral Fellow jointly cultivated by The Chinese University of Hong Kong, Hong Kong, and the Dalian University of Technology, and also a Visiting Scholar with the Department of Computer Science and Engineering,

Washington University in St. Louis, St. Louis, MO, USA, from 2018 to 2019. Since 2019, he has been a Professor with the Department of Ocean Remote Sensing, National Marine Environmental Monitoring Center, Dalian, China. He is currently a Professor with the School of Control Science and Engineering, Dalian University of Technology. He has authored or coauthored three books and more than 100 scientific papers in international journals and conference proceedings, such as *IEEE TRANSACTIONS ON FUZZY SYSTEMS*, *IEEE TRANSACTIONS ON NEURAL NETWORKS AND LEARNING SYSTEMS*, *IEEE TRANSACTIONS ON GEOSCIENCE AND REMOTE SENSING*, *IEEE JOURNAL OF SELECTED TOPICS IN APPLIED EARTH OBSERVATIONS AND REMOTE SENSING*, *IEEE GEOSCIENCE AND REMOTE SENSING LETTERS*, *PATTERN RECOGNITION*, etc. His research interests include marine SAR image processing, polarimetric SAR, deep learning neural networks, and heuristic swarm intelligent optimization.

Dr. Fan is the Program Chair, Workshop Chair, Publicity Chair, and the Local Arrangement Chair of several international conferences, such as the International Symposium on Neural Networks, the International Conference on Information Society and Technology, and the International Conference on Intelligent Control and Information Processing.